13. C. T. Black, *Appl. Phys. Lett.* **87**, 163116 (2005).
14. T. Thurn-Albrecht *et al.*, *Science* **290**, 2126 (2000).
15. K. Naito, H. Hieda, M. Sakurai, Y. Kamata, K. Asakawa, *IEEE Trans. Magn.* **38**, 1949 (2002).
16. Y. S. Jung, W. Jung, H. L. Tuller, C. A. Ross, *Nano Lett.* **8**, 3776 (2008).
17. S. Ji *et al.*, *Adv. Mater.* **23**, 3692 (2011).
18. S.-M. Park, G. S. W. Craig, Y.-H. La, P. F. Nealey, *Macromolecules* **41**, 9124 (2008).
19. S. M. Park, G. S. W. Craig, Y.-H. La, H. H. Solak, P. F. Nealey, *Macromolecules* **40**, 5084 (2007).
20. K. Ch. Daoulas *et al.*, *Phys. Rev. Lett.* **96**, 036104 (2006).
21. H. Jung *et al.*, *ACS Nano* **5**, 6164 (2011).
22. F. Rose, J. K. Bosworth, E. A. Dobisz, R. Ruiz, *Nanotechnology* **22**, 035603 (2011).
23. E. Kim *et al.*, *Soft Matter* **4**, 475 (2008).
24. Y. Wu *et al.*, *Nat. Mater.* **3**, 816 (2004).
25. K. Shin *et al.*, *Science* **306**, 76 (2004).
26. C. S. Henkee, E. L. Thomas, L. J. Fetters, *J. Mater. Sci.* **23**, 1685 (1988).
27. B. Yu, B. Li, Q. Jin, D. Ding, A. C. Shi, *Soft Matter* **7**, 10227 (2011).
28. R. Ruiz, E. Dobisz, T. R. Albrecht, *ACS Nano* **5**, 79 (2011).
29. W. A. Phillip, M. A. Hillmyer, E. L. Cussler, *Macromolecules* **43**, 7763 (2010).
30. See supplementary materials on *Science* Online.
31. J. K. W. Yang *et al.*, *Nat. Nanotechnol.* **5**, 256 (2010).
32. M. P. Stoykovich *et al.*, *Science* **308**, 1442 (2005).
33. M. P. Stoykovich *et al.*, *ACS Nano* **1**, 168 (2007).
34. Q. Peng, Y.-C. Tseng, S. B. Darling, J. W. Elam, *ACS Nano* **5**, 6 (2011).

Acknowledgments: Supported by a fellowship from NGS Singapore (A.T.K.G.), the Semiconductor Research Corporation, the Center on Functional Engineered and Nano Architectonics, Nanoelectronics Research Initiative, Singapore-MIT Alliance, Tokyo Electron, and Taiwan Semiconductor Manufacturing Company. We thank M. Mondol and J. Daley for technical assistance. A.T.K.G. would like to express his profound gratitude to T. C. Chong and S. N. Piramanayagam for their support. The Research Laboratory of Electronics Scanning-Electron-Beam Lithography Facility at MIT provided facilities for this work. A patent titled "Removable Templates for Directed Self-Assembly" has been filed with MIT.

Supplementary Materials

www.sciencemag.org/cgi/content/full/336/6086/1294/DC1
Materials and Methods
Figs. S1 to S18
References (*35–38*)

27 December 2011; accepted 20 April 2012
10.1126/science.1218437

Titanium and Zinc Oxide Nanoparticles Are Proton-Coupled Electron Transfer Agents

Joel N. Schrauben, Rebecca Hayoun, Carolyn N. Valdez, Miles Braten, Lila Fridley, James M. Mayer*

Oxidation/reduction reactions at metal oxide surfaces are important to emerging solar energy conversion processes, photocatalysis, and geochemical transformations. Here we show that the usual description of these reactions as electron transfers is incomplete. Reduced TiO_2 and ZnO nanoparticles in solution can transfer an electron and a proton to phenoxyl and nitroxyl radicals, indicating that e^- and H^+ are coupled in this interfacial reaction. These proton-coupled electron transfer (PCET) reactions are rapid and quantitative. The identification of metal oxide surfaces as PCET reagents has implications for the understanding and development of chemical energy technologies, which will rely on e^-/H^+ coupling.

Oxidation/reduction reactions of metal oxide materials (MO_x) play a key role in emerging energy technologies, as well as other processes such as photocatalytic wastewater remediation and self-cleaning surfaces (*1*) and geochemical redox formation and dissolution of minerals (*2*). These interfacial (solid/solution) redox processes are generally described just in terms of electron transfer (ET). For instance, the extensive literature on photochemical and electrochemical water splitting by MO_x is focused on the ET between surface-bound species and the valence and conduction bands of the solid. In dye-sensitized solar cells (DSSCs), the excited state of a dye injects an e^- into nanocrystalline TiO_2 (*3*). All of these disparate processes are affected by proton activity (the pH of aqueous interfaces), indicating a role for H^+. Here, we report well-characterized examples of reduced TiO_2 and ZnO nanoparticles (TiO_2/e^- and ZnO/e^-) reacting by proton-coupled electron transfer [PCET (*4*)]. TiO_2 and ZnO have been extensively studied from both fundamental and technological

Department of Chemistry, University of Washington, Seattle WA 98195, USA.

*To whom correspondence should be addressed. E-mail: mayer@chem.washington.edu

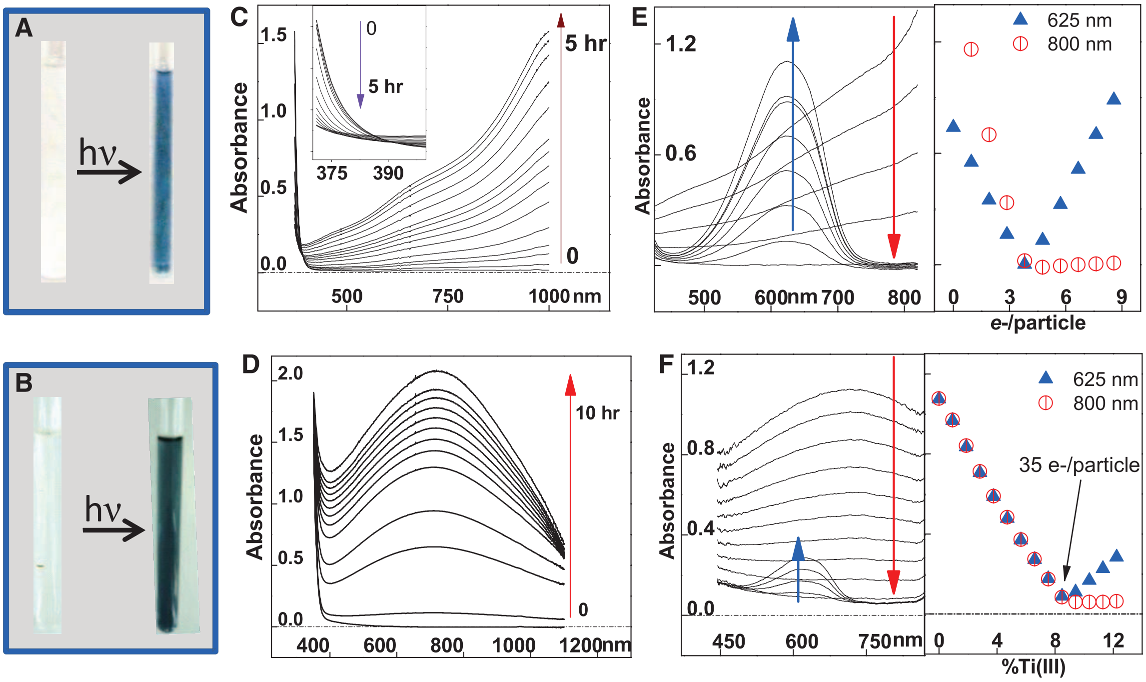

Fig. 1. Pictures of as-prepared and reduced (**A**) ZnO and (**B**) amorphous TiO_2 nanoparticles in toluene. UV-visible spectra of solutions of (**C**) ZnO (20-μM particles, 3.9-nm diameter) and (**D**) amorphous TiO_2 (51 μM, 3 nm) during irradiation with a 200-W Hg/Xe lamp. $^tBu_3ArO^\bullet$ titrations of (**E**) ZnO/e^- (0.51 mM, 3.9 nm) after 30 min of irradiation and (**F**) TiO_2/e^- (51 μM, 3 nm) after 10 min of irradiation.

perspectives [nearly 58,000 publications on TiO_2 alone (5)], and well-characterized nanoparticle systems have been described. The demonstration that these reduced oxides can transfer both electrons and protons expands the traditional view of interfacial redox reactions. The occurrence of interfacial PCET brings together previous electrochemical, photochemical, and photocatalytic reports of H^+/e^- coupling in TiO_2 (*1*, *3*, *6*–*9*) and ZnO (*10*), as discussed below. PCET is likely a common theme for MO_x reactivity in the presence of protons (*11*, *12*).

Dodecylamine-capped ZnO nanocrystals (3 to 6 nm in diameter) and oleic acid–capped amorphous and anatase TiO_2 particles (3 and 5 nm in diameter, respectively) were prepared and characterized by well-known procedures (*13*–*15*). Ultraviolet (UV) irradiation of these materials forms electron/hole pairs (excitons), and rapid quenching of the holes by oxidation of organic species at the surface (*1*) leaves extra electrons in the particles. Toluene solutions of these ZnO/e^- and TiO_2/e^- particles, as previously reported, are long-lived in the absence of air; are blue or purple/black, respectively, because of optical and near-infrared absorbances (Fig. 1, A to D); and have characteristic electron paramagnetic resonance (EPR) spectra (*9*, *16*–*19*). The added electrons occupy delocalized, conduction band-like orbitals in ZnO/e^- (*19*, *20*), whereas in TiO_2/e^- they are much more localized on a few Ti atoms (*11*).

Addition of the stable 2,4,6-tri-*tert*-butylphenoxyl radical ($^t\mathrm{Bu_3ArO^{\bullet}}$) to air-free toluene solutions of ZnO/e^- or TiO_2/e^- (amorphous or anatase) yields the oxidized particles and the corresponding phenol $^t\mathrm{Bu_3ArOH}$, as indicated by ^1H nuclear magnetic resonance (NMR), EPR, optical spectroscopies, and gas chromatography (GC) (Fig. 2A). A similar reaction is observed for irradiated anaerobic slurries of Aeroxide P25 TiO_2 (Evonik Industries AG, Essen, Germany), a commercially available anatase with average particle diameter ~20 nm, so this result is not limited to organic-capped soluble nanoparticles. ZnO/e^- and TiO_2/e^- are also oxidized by the nitroxyl radical 2,2,6,6-tetramethyl-piperidin-1-yl-oxyl (TEMPO) to give the reduced hydroxyl amine TEMPOH. The organic radicals do not react with nonreduced particles, particles that have not been irradiated, or particles that have been reduced and then reoxidized by air. These reactions (Eqs. 1 and 2) occur in toluene, a solvent without acidic protons. Therefore, the formation of $^t\mathrm{Bu_3ArOH}$ from $^t\mathrm{Bu_3ArO^{\bullet}}$, and TEMPOH from TEMPO, must involve transfer of e^- and H^+ from the particles to the organic radical; the proton is explicitly shown in the balanced Eqs. 1 and 2. Reduced TiO_2 has previously been shown to accomplish multielectron/multiproton reductions, but often the solvent (typically water) was assumed to provide the protons (*9*, *17*, *18*).

$$H^+\text{-}TiO_2/e^- + XO^{\bullet} \rightarrow TiO_2 + XOH \qquad (1)$$

$$H^+\text{-}ZnO_2/e^- + XO^{\bullet} \rightarrow ZnO_2 + XOH$$

$$XO^{\bullet} = {}^t\mathrm{Bu_3ArO^{\bullet}},\ \mathrm{TEMPO} \qquad (2)$$

The active protons likely come both from the particle syntheses and from the photochemical charging. The particles were prepared hydrolytically and were not calcined, so surface hydroxyl groups are undoubtedly present. The particles are capped by organic ligands (vide supra) and likely contain residual solvents from syntheses, particularly ethanol. Analyses of ZnO/e^- solutions by GC and GC–mass spectroscopy (GC-MS) show that quenching of the photolytically formed hole yields one primary product: the imine from condensation of dodecylamine and acetaldehyde, the latter from $2e^-/2H^+$ oxidation of ethanol (Eq. 3, R = dodecyl). The identity of the product was confirmed by independent synthesis. Thus, protons are formed commensurate with the electrons in the reduced particles. (No photocharging products derived from the toluene solvent have been observed.)

$$2h^+ + CH_3CH_2OH + H_2NR \rightarrow CH_3CH{=}NR + H_2O + 2H^+ \qquad (3)$$

Titrations of ZnO/e^- solutions show a gradual disappearance of the ZnO/e^- absorbance and then, after the endpoint, appearance of the spectrum of the excess $^t\mathrm{Bu_3ArO^{\bullet}}$ (Fig. 1E). Addition of a small excess of $^t\mathrm{Bu_3ArO^{\bullet}}$ causes disappearance of the ZnO/e^- resonance in the EPR spectrum and appearance of the signal for the remaining $^t\mathrm{Bu_3ArO^{\bullet}}$. Titrations with the pure electron acceptor decamethylferrocenium ($Cp^*{}_2Fe^+$) are very similar, and titrations of different aliquots of the same ZnO/e^- solution with $Cp^*{}_2Fe^+$ and $^t\mathrm{Bu_3ArO^{\bullet}}$ give the same "concentration of electrons" within the ±10% uncertainty of the titrations (from repetitive measurements; fig. S4). Thus, all of the spectroscopically visible conduction band (CB) electrons in ZnO/e^- can be removed either as e^-, with $Cp^*{}_2Fe^+$, or as e^- accompanied by H^+ with $^t\mathrm{Bu_3ArO^{\bullet}}$. The titration results, together with the total metal concentration and the average particle diameter, give the average number of electrons per particle (n_{e^-}); 3.9-nm ZnO

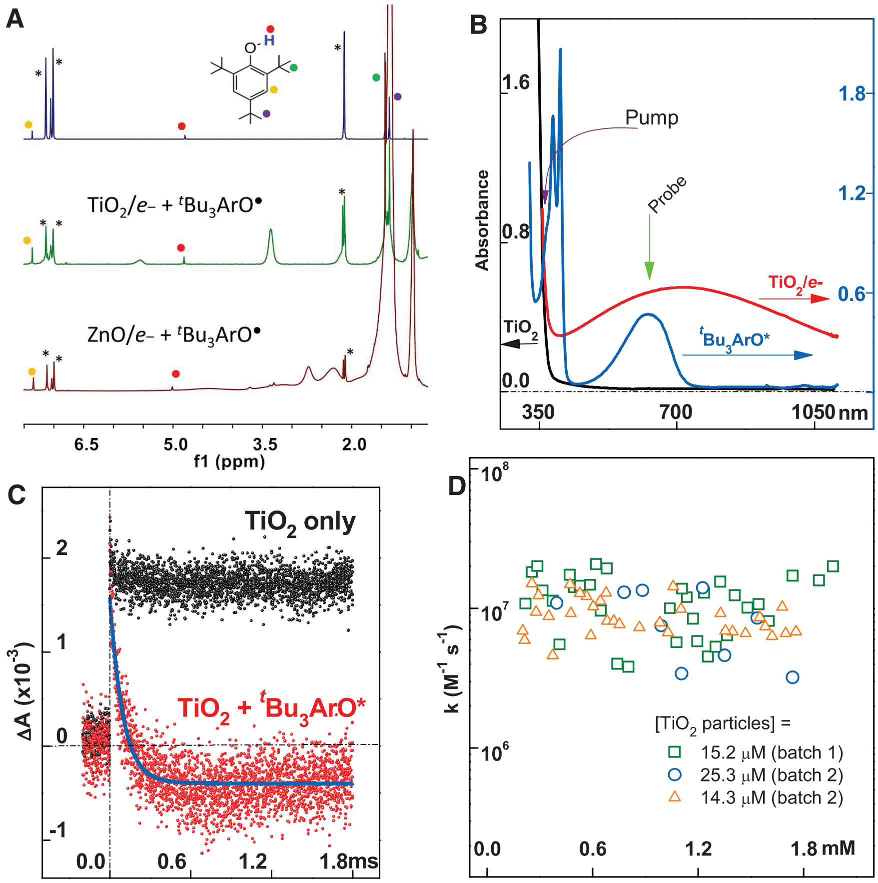

Fig. 2. (**A**) The ^1H NMR spectra in toluene-d_8 of (top) $^t\mathrm{Bu_3ArOH}$, (middle) amorphous TiO_2 (50 μM, ~3 nm, irradiated for 30 min) and $^t\mathrm{Bu_3ArO^{\bullet}}$ (45 equivalents per particle), and (bottom) the corresponding reaction for ZnO (2.5 equivalents $^t\mathrm{Bu_3ArO^{\bullet}}$, 1.9 mM particles, ~4 nm, irradiated for 30 min), showing formation of $^t\mathrm{Bu_3ArOH}$ (circles) (asterisks indicate solvent peaks; peaks of the particle capping groups are unlabeled). (**B**) Optical spectra of as-prepared TiO_2 particles (black), TiO_2/e^- (red), and $^t\mathrm{Bu_3ArO^{\bullet}}$ (blue); the wavelengths of the exciting laser (pump) and monitoring position (probe) are indicated. (**C**) Typical kinetic traces monitoring the absorbance at 620 nm as a function of time after the laser flash: black points, TiO_2 only; red points, TiO_2 and $^t\mathrm{Bu_3ArO^{\bullet}}$ (0.78 mM) with fit to second-order kinetics (supplementary material pp. 7 and 8, figs. S10 to S14, and table S1). (**D**) Plot of second-order rate constants *k* [e.g., from (**C**)] versus concentration of $^t\mathrm{Bu_3ArO^{\bullet}}$.

particles irradiated for 30 min typically show $n_{e^-} \approx 4$, consistent with prior work (*19*).

Titrations of $\mathrm{TiO_2}/e^-$ solutions behave similarly, giving the same value of n_{e^-} within error with use of either $^t\mathrm{Bu_3ArO}^\bullet$ or ferrocenium ($\mathrm{Cp_2Fe^+}$) (fig. S5). The derived extinction coefficient per electron ε_{e^-} (700 nm) = 633 ± 70 $\mathrm{M^{-1}\ cm^{-1}}$ is similar to that in other reduced $\mathrm{TiO_2}$ systems (*18*) (±1σ error, from the data in fig. S5). Irradiation of the amorphous particles was found to cause extensive reduction, $n_{e^-} \approx 45$ per 3-nm particle after 1 hour based on the above ε_{e^-}. Continued irradiation results in slower additional reduction, up to $n_{e^-} \approx 72$ after 10 hours. These values correspond, respectively, to reduction of 10% and 16% of all the $\mathrm{Ti^{4+}}$ ions to $\mathrm{Ti^{3+}}$. Anatase $\mathrm{TiO_2}$ nanocrystals are photochemically reduced to a smaller extent, ~2% $\mathrm{Ti^{3+}}$ ($n_{e^-} \approx 40$ per 5-nm nanocrystal) after >4 hours of irradiation. For comparison, the nanostructured $\mathrm{TiO_2}$ in an operating dye-sensitized solar cell is ~0.03% reduced (usually reported as ~10^{18} $e^-/\mathrm{cm^3}$) (*21*), and the ZnO/e^- particles above could be considered 0.3% reduced. The greater reduction of the $\mathrm{TiO_2}$ particles is likely due in part to the localized nature of the reduced sites, and the very extensive reduction of the amorphous $\mathrm{TiO_2}$ is attributed to the ability of the charge-balancing protons to be close to the added electrons.

The kinetics of the PCET reactions have been interrogated with flash photolysis using ~5-ns pulses of 355-nm light. With amorphous $\mathrm{TiO_2}$ particles in the absence of an oxidant, irradiation causes an increased absorbance at 620 nm within ~10 ns that does not decay over several ms (Fig. 2, B and C, black points), indicating the formation of a stable $\mathrm{TiO_2}/e^-$ solution (Fig. 1C) (*18*, *22*, *23*). When the particles are excited in the presence of $^t\mathrm{Bu_3ArO}^\bullet$, this feature is observed transiently but decays on a ~200-μs time scale to an absorbance lower than the initial value (Fig. 2C, red points). The decay is due to consumption of both $\mathrm{TiO_2}/e^-$ and $^t\mathrm{Bu_3ArO}^\bullet$. Kinetic data over a range of concentrations of $^t\mathrm{Bu_3ArO}^\bullet$ and $\mathrm{TiO_2}$ particles follow second-order kinetics and yield the bimolecular rate constant (1.0 ± 0.4) × 10^7 $\mathrm{M^{-1}\ s^{-1}}$ (this value is the average ± 1σ for many measurements between 0.1 and 2.0 mM $^t\mathrm{Bu_3ArO}^\bullet$ with data from two different batches of particles; Fig. 2D and table S1). Reactions of the anatase particles occur with a similar rate constant of (1.5 ± 0.4) × 10^7 $\mathrm{M^{-1}\ s^{-1}}$ (from six measurements between 0.2 and 0.7 mM $^t\mathrm{Bu_3ArO}^\bullet$; fig. S10). These are fast reactions, within ~10^3 of the estimated diffusion limit (see supplementary materials, p. 9). Oxidations of amorphous $\mathrm{TiO_2}/e^-$ with the pure electron acceptors methylviologen or $\mathrm{Cp^*{}_2Fe^+}$ proceed even faster (>10^7 $\mathrm{M^{-1}\ s^{-1}}$, fig. S11). The kinetics of ZnO/e^- and $^t\mathrm{Bu_3ArO}^\bullet$ were measured similarly, monitoring the recovery of the bleached ZnO band edge. Reactions of two different batches of ZnO/e^- particles with $^t\mathrm{Bu_3ArO}^\bullet$ gave rate constants of (3.0 ± 0.6) × 10^7 $\mathrm{M^{-1}\ s^{-1}}$ and (6.9 ± 1.3) × 10^6 $\mathrm{M^{-1}\ s^{-1}}$ (from 13 measurements between 0.5 and 2 mM $^t\mathrm{Bu_3ArO}^\bullet$, fig. S12). When an excess of the dodecylamine capping group was added to the latter batch, *k* was reduced by nearly a factor of two (table S1). This suggests that the oxidant must reach the surface of the particle and that different dodecylamine surface coverage may explain the variation in *k* between batches of particles. The reactions of TEMPO are much slower than those of $^t\mathrm{Bu_3ArO}^\bullet$: Amorphous $\mathrm{TiO_2}/e^-$ + TEMPO has a second-order rate constant just one-thousandth as high [(1.1 ± 0.5) × 10^4 $\mathrm{M^{-1}\ s^{-1}}$] (from six measurements at 25 mM TEMPO, fig. S13), and for one batch of ZnO particles (fig. S14) the rate constant for reaction with TEMPO was nearly a factor of 40,000 smaller.

These PCET reactions are unlikely to proceed by a mechanism of initial outer-sphere ET, even though this is the common proposal for interfacial redox reactions. The reduction of TEMPO to its anion is in particular thermodynamically very difficult (*24*), and the formation of either $^t\mathrm{Bu_3ArO^-}$ or $\mathrm{TEMPO^-}$ is unfavorable in the nonpolar toluene solvent used. $^t\mathrm{Bu_3ArO}^\bullet$ or TEMPO could bind to a coordinatively unsaturated surface metal center, followed by protonation to give free XOH. This would be analogous to nitroxyl radicals binding to molecular $\mathrm{Ti^{3+}}$ complexes such as $\mathrm{Cp_2Ti^{III}Cl}$ to form $\mathrm{Ti^{4+}}$-nitroxide species (*25*–*27*) (Cp = η^5-$\mathrm{C_5H_5}$). However, a high density of unsaturated titanium centers seems unlikely given the hydrolytic synthesis of the particles and the tightly held oleate capping ligands. In addition, $\mathrm{XO}^\bullet$ binding would be expected to be more rapid for the less sterically encumbered TEMPO radical, but this radical reacts 10^3 to 10^4 times slower than $^t\mathrm{Bu_3ArO}^\bullet$. The reactions thus more likely proceed by a concerted proton-electron transfer (CPET), equivalently called hydrogen atom ($\mathrm{H}^\bullet$) transfer (HAT). Both $^t\mathrm{Bu_3ArO}^\bullet$ and TEMPO are common $\mathrm{H}^\bullet$ abstractors (*24*). The faster reactions of $^t\mathrm{Bu_3ArO}^\bullet$ are consistent with a HAT mechanism because the O–H bond formed by $^t\mathrm{Bu_3ArO}^\bullet$ is 11.5 kcal $\mathrm{mol^{-1}}$ stronger than that formed by TEMPO (*24*).With use of our model of bimolecular HAT rate constants (k_{HAT}) based on the Marcus cross relation (*28*), this greater driving force should be associated with a ~10^4 faster k_{HAT}, in good agreement with the measured values. These reactions of metal oxide particles are therefore analogous to HAT from molecular $\mathrm{Ti^{3+}}$-aquo complexes to carbon radicals $\mathrm{R}^\bullet$ (Eq. 4) (*29*).

$$\mathrm{Cp_2(Cl)Ti^{III}(OH_2)} + \mathrm{R}^\bullet \rightarrow \mathrm{Cp_2(Cl)Ti^{IV}(OH)} + \mathrm{R\text{-}H}$$
$$k = 1.0 \times 10^5\ \mathrm{M^{-1}\ s^{-1}} \qquad (4)$$

The demonstration here that MO_x particles can react by PCET provides an expanded view of interfacial charge transfer reactions and the involvement of protons. From an energetic perspective, proton activity (pH in aqueous solutions) is known to strongly modulate the effective CB energy (E_{CB}) of bulk metal oxides. Although this behavior has traditionally been ascribed to changes in surface protonation (*30*), recent work indicates that each electron added to the oxide is accompanied by a proton (*3*, *6*–*8*, *31*–*34*). Most notably, Hupp and co-workers showed proton uptake upon electrochemical reduction of $\mathrm{TiO_2}$ (*6*, *7*). This is analogous to the addition of both e^- and $\mathrm{Li^+}$ upon charging of a lithium battery anode (*6*, *33*, *35*) and to $\mathrm{H}^\bullet$-doped ZnO and $\mathrm{TiO_2}$ (*1*, *9*, *10*). These and other studies indicate that reduced and protonated metal oxides are formed under a variety of electrochemical and chemical conditions, not only by the photochemical charging route used here. The thermochemical coupling between E_{CB} and pH is related to the $e^-/\mathrm{H^+}$ (PCET) reactivity described here, and together they have broad implications. Transfer of e^- and $\mathrm{H^+}$ to or from a surface requires at least a partially localized description, in contrast to the pure delocalized band-structure pictures typically used for interfacial ET and for PCET reactions in which interfacial ET is coupled to proton movements within a solute or solvent (*36*–*38*). For instance, the PCET reducing power of the particles studied here reflects their ability to donate e^- and $\mathrm{H^+}$ together, not just their ability to donate electrons, and is thus only indirectly related to the E_{CB} or Fermi energy (just as the potential of a lithium battery anode is not the E_{CB} of the oxide). The ability to transfer e^- and $\mathrm{H^+}$ together should be advantageous in metal oxide catalysis, electrocatalysis, and photocatalysis of reactions such as water oxidation ($\mathrm{2H_2O \rightarrow O_2 + 4H^+ + 4}e^-$), because moving the two particles together can avoid high-energy chemical intermediates (*4*).

References and Notes

1. A. Fujishima, X. Zhang, D. Tryk, *Surf. Sci. Rep.* **63**, 515 (2008).
2. M. Pourbaix, *Atlas of Electrochemical Equilibria in Aqueous Solutions* (Pergamon, New York, 1966).
3. S. Ardo, G. J. Meyer, *Chem. Soc. Rev.* **38**, 115 (2009).
4. S. Hammes-Schiffer, *Chem. Rev.* **110** (12), 6937 (2010).
5. P. V. Kamat, *J. Phys. Chem. Lett.* **2**, 839 (2011).
6. L. A. Lyon, J. T. Hupp, *J. Phys. Chem.* **99**, 15718 (1995).
7. L. A. Lyon, J. T. Hupp, *J. Phys. Chem. B* **103**, 4623 (1999).
8. G. Redmond, D. Fitzmaurice, *J. Phys. Chem.* **97**, 1426 (1993).
9. X. Chen, L. Liu, P. Y. Yu, S. S. Mao, *Science* **331**, 746 (2011); 10.1126/science.1200448.
10. J. K. Park, K. Won Lee, H. Kweon, C. E. Lee, *Appl. Phys. Lett.* **98**, 102502 (2011).
11. X. Chen, S. S. Mao, *Chem. Rev.* **107**, 2891 (2007).
12. A. J. Bard, *J. Am. Chem. Soc.* **132**, 7559 (2010).
13. Materials and methods are available as supplementary materials on *Science* Online.
14. D. A. Schwartz, D. R. Gamelin, *Proc. SPIE Int. Soc. Opt. Eng.* **5224**, 1 (2003).
15. P. D. Cozzoli, A. Kornowski, H. Weller, *J. Am. Chem. Soc.* **125**, 14539 (2003).
16. I. A. Shkrob, S. D. Chemerisov, *J. Phys. Chem. C* **113**, 17138 (2009).
17. X.-X. Zou *et al.*, *Chem. Commun. (Camb.)* **46**, 2112 (2010).
18. H. H. Mohamed, C. B. Mendive, R. Dillert, D. W. Bahnemann, *J. Phys. Chem. A* **115**, 2139 (2011).
19. W. K. Liu *et al.*, *Phys. Rev. Lett.* **98**, 186804 (2007).
20. A. Germeau *et al.*, *Phys. Rev. Lett.* **90**, 097401 (2003).
21. B. C. O'Regan, J. R. Durrant, *Acc. Chem. Res.* **42**, 1799 (2009).
22. U. Koelle, J. Moser, M. Graetzel, *Inorg. Chem.* **24**, 2253 (1985).
23. D. Bahnemann, A. Henglein, J. Lilie, L. Spanhel, *J. Phys. Chem.* **88**, 709 (1984).

24. J. J. Warren, T. A. Tronic, J. M. Mayer, *Chem. Rev.* **110**, 6961 (2010).
25. M. K. Mahanthappa, K.-W. Huang, A. P. Cole, R. M. Waymouth, *Chem. Commun. (Camb.)* **2002**, 502 (2002).
26. M. K. Mahanthappa, A. P. Cole, R. M. Waymouth, *Organometallics* **23**, 836 (2004).
27. K. Schröder *et al.*, *Organometallics* **27**, 1859 (2008).
28. J. M. Mayer, *Acc. Chem. Res.* **44**, 36 (2011).
29. J. Jin, M. Newcomb, *J. Org. Chem.* **73**, 7901 (2008).
30. S. Morrison, *Electrochemistry at Semiconductor and Oxidized Metal Electrodes* (Plenum, New York, 1980).
31. B. Enright, G. Redmond, D. Fitzmaurice, *J. Phys. Chem.* **98**, 6195 (1994).
32. F. Marken, A. S. Bhambra, D.-H. Kim, R. J. Mortimer, S. J. Stott, *Electrochem. Commun.* **6**, 1153 (2004).
33. M. Zukalova, M. Kalbáč, L. Kavan, I. Exnar, M. Graetzel, *Chem. Mater.* **17**, 1248 (2005).
34. A. Minguzzi, F.-R. F. Fan, A. Vertova, S. Rondinini, A. J. Bard, *Chem. Sci.* **3**, 217 (2012).
35. Y. Ren, L. J. Hardwick, P. G. Bruce, *Angew. Chem. Int. Ed.* **49**, 2570 (2010).
36. C. Venkataraman, A. V. Soudackov, S. Hammes-Schiffer, *J. Phys. Chem. C* **114**, 487 (2010).
37. H. Petek, J. Zhao, *Chem. Rev.* **110**, 7082 (2010).
38. C. Costentin, *Chem. Rev.* **108**, 2145 (2008).

Acknowledgments: Materials and methods and additional figures are presented in the supplementary materials on *Science* Online. We are grateful for financial support from the University of Washington, the American Chemical Society Petroleum Research Fund (51178-ND3), and the U.S. NSF (CHE-1151726). This research is also supported in part by the Department of Energy Office of Science Graduate Fellowship Program, made possible in part by the American Recovery and Reinvestment Act of 2009, administered by Oak Ridge Institute for Science and Education–Oak Ridge Associated Universities under contract no. DE-AC05-06OR23100, and in part by the NSF Center for Enabling New Technologies through Catalysis. We especially thank D. Gamelin, members of the Gamelin laboratory, and L. Maibaum for very valuable discussions.

Supplementary Materials

www.sciencemag.org/cgi/content/full/336/6086/1298/DC1
Materials and Methods
Supplementary Text
Figs. S1 to S14
Table S1
References (*39*–*54*)

7 February 2012; accepted 10 April 2012
10.1126/science.1220234

Interglacial Hydroclimate in the Tropical West Pacific Through the Late Pleistocene

A. N. Meckler,[1,2]* M. O. Clarkson,[3] K. M. Cobb,[4] H. Sodemann,[5] J. F. Adkins[1]

Records of atmospheric carbon dioxide concentration (P_{CO_2}) and Antarctic temperature have revealed an intriguing change in the magnitude of interglacial warmth and P_{CO_2} at around 430,000 years ago (430 ka), but the global climate repercussions of this change remain elusive. Here, we present a stalagmite-based reconstruction of tropical West Pacific hydroclimate from 570 to 210 ka. The results suggest similar regional precipitation amounts across the four interglacials contained in the record, implying that tropical hydroclimate was insensitive to interglacial differences in P_{CO_2} and high-latitude temperature. In contrast, during glacial terminations, drying in the tropical West Pacific accompanied cooling events in northern high latitudes. Therefore, the tropical convective heat engine can either stabilize or amplify global climate change, depending on the nature of the climate forcing.

The study of past interglacial climates provides valuable insight into natural climate variability under conditions roughly similar to those of the present day, but with differences in atmospheric carbon dioxide concentration (P_{CO_2}) (*1*) and astronomic forcing. Especially intriguing is a step-like increase in interglacial Antarctic temperature (*2*), global ice melting (*3*), and P_{CO_2} (*4*, *5*) that took place at roughly 430,000 years ago (430 ka) and is referred to as the Mid-Brunhes Event (MBE). To understand the underlying cause of this shift toward warmer interglacials, it is crucial to establish the global signature of interglacial climates during that time, but sufficiently long records, especially from low latitudes and terrestrial archives, are sparse. Because P_{CO_2} and ice cover affect the planet's radiative balance, a global change in interglacial climate at the MBE might be expected. Although many marine sea surface temperature (SST) reconstructions from around the globe show qualitatively similar changes to those observed in Antarctica (*6*), the few available lower-latitude SST reconstructions (*7*–*9*) from this time period do not show the same consistent increase in post-MBE interglacial temperatures. Given that many models simulate strong dynamical links between high-latitude and tropical climate [e.g., (*10*)], more tropical records are required to test and improve our understanding of low-latitude climate sensitivity to a range of different forcing factors.

Here, we present stalagmite records from northern Borneo (4°N, 115°E; fig. S1) that span several glacial-to-interglacial cycles and include the MBE. We reconstruct Warm Pool hydroclimate from the oxygen isotope ($\delta^{18}O$) variability recorded in three stalagmites with overlapping growth periods. Borneo lies in the West Pacific Warm Pool, which is an important heat and moisture source for higher latitudes (*11*). Although there is little seasonality in modern rainfall amount at our site, the isotopic composition of precipitation varies seasonally by up to 2 to 3‰ (*12*), with the most enriched $\delta^{18}O$ values occurring in February and March, when the intertropical convergence zone (ITCZ) is furthest south of our site. However, on interannual time scales, the El Niño–Southern Oscillation (ENSO) phenomenon dominates both precipitation amount and $\delta^{18}O$, with El Niño events resulting in large-scale drying and rainfall $\delta^{18}O$ that is roughly 5 to 6‰ higher than average (*12*). Two recent studies of water isotopes in the same area conclude that regional (much more than local) rainfall amount is the main driver for rainfall $\delta^{18}O$ variability on intraseasonal and longer time scales today (*13*) and during modeled millennial-scale events in the past (*14*).

We analyzed stalagmites from three different caves in Gunung Mulu and Gunung Buda National Parks, each about 5 to 10 km apart. The stalagmites were dated by ^{238}U-^{234}U-^{230}Th measurements (*15*) and cover the time period from 570 (±20) ka to 210 (±10) ka [from marine isotope stage (MIS) 13 to the beginning of MIS7], with some gaps due to hiatuses. Sample GC08 covers the whole time period, whereas samples Squeeze1 and WR5 yield shorter records that overlap GC08. In comparison to other cave systems, dating of these stalagmites is challenging due to their unusually low $^{234}U/^{238}U$ ratios and/or low U concentrations (fig. S4 and tables S1 to S3). The old age of the samples exacerbates these dating issues. Furthermore, there is evidence that slight open-system exchange of U has affected sample GC08, requiring us to model the ages in this stalagmite by assuming a constant initial $^{234}U/^{238}U$ ratio (*15*). Varying detrital ^{230}Th contamination cannot explain the age reversals in this stalagmite, owing to the short half-life of ^{230}Th compared to the age of our samples (*15*). The error assigned to the assumed constant initial $^{234}U/^{238}U$ ratio leads to increased age uncertainty in the GC08 chronology, with individual age errors ranging from ±9200 to ±13,500 years (2σ; table S1), limiting our ability to compare the millennial-scale timing of climate change in Borneo with other records. The age constraints are sufficient, however, to identify each interglacial stage, which is the main focus of this study. In sample WR5, open-system alteration might also have occurred but cannot be corrected for (*15*). The $\delta^{18}O$ record from this stalagmite therefore

---

[1] Geological and Planetary Science Department, California Institute of Technology, Pasadena, CA, USA. [2] Geological Institute, ETH Zurich, Switzerland. [3] School of GeoSciences, University of Edinburgh, Edinburgh EH9 3JW, UK. [4] School of Earth and Atmospheric Sciences, Georgia Institute of Technology, Atlanta, GA 30332, USA. [5] Institute for Atmosphere and Climate, ETH Zurich, Switzerland.

*To whom correspondence should be addressed. E-mail: nele.meckler@erdw.ethz.ch